Supplemental Materials

Liquid metal assisted dual hydroxide heterostructures of carbonyl iron powder for multifunctional electromagnetic wave absorption

Yunpeng Li[1,2], Shenghao Yue[3], Ting-An He[1,2], Jiabao Zang[1,2], Xuejun Bai[1,2], Lihong Gao[1,2,4], Zhuang Ma[1,2,4], Qi Cao[3], Miao Jiang[1,2,4,5]

[1]School of Materials Science and Engineering, Beijing Institute of Technology, Beijing 100081, China.
[2]National Key Laboratory of Science and Technology on Materials under Shock and Impact, Beijing Institute of Technology, Beijing 100081, China.
[3]Key Laboratory of Energy Thermal Conversion and Control of Ministry of Education, Key Laboratory of Functional Polymers for Sustainability of Jiangsu Province, School of Energy and Environment, Southeast University, Nanjing 210096, Jiangsu, China.
[4]Materials Intelligent Innovation Laboratory (MIIL), Beijing Institute of Technology, Zhuhai 519088, Guangdong, China.
[5]Yangtze Delta Region Academy in Jiaxing, Beijing Institute of Technology, Jiaxing 314000, Zhejiang, China.

Correspondence to: Prof. Miao Jiang, School of Materials Science and Engineering, Beijing Institute of Technology, Beijing 100081, China. E-mail: jiangmiao@bit.edu.cn

This Word includes:

Section S1: Particle Size Distribution Analysis

Section S2: Dimensions Analysis of the Nanorod Shell

Section S3: SEM Characterization of Control Samples

Section S4: Comparative EMW Absorption Performance of Control Samples

Section S5: Electromagnetic Parameters of Samples at Different Ultrasonication Times

Section S6: Quantitative Analysis of Impedance Matching in the Absorption-Relevant Region

Section S7: Reflection-Loss Performance at Reduced Filler Loadings

Section S8: Separation of Dielectric Loss Components Based on Debye Relaxation Theory

Section S9: Tafel Curve Calculation

Section S1: Particle Size Distribution Analysis

Figure S1 illustrates the particle size distributions of pristine CIP, CIP@C, and the CIP@C@LM composite. Following the successive assembly of the shell materials, the average particle size progressively increases from 2.36 μm for pristine CIP to 2.47 μm for CIP@C, and finally reaches 2.64 μm for the CIP@C@LM heterostructure. Concurrently, the size distribution becomes more concentrated; the fraction of particles distributed within the predominant 2–3 μm range gradually rises from 0.46 (pristine CIP) to 0.48 (CIP@C) and 0.53 (CIP@C@LM). This synchronized increase in both average size and dimensional uniformity explicitly corroborates the successful and uniform encapsulation of the core-shell architecture.

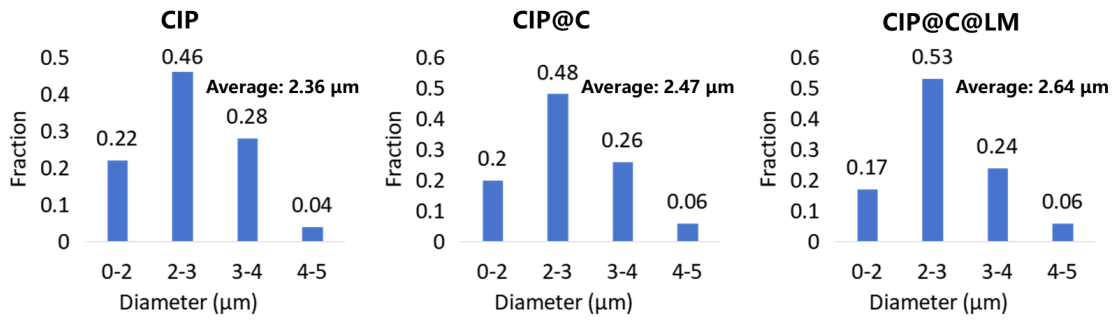

Figure S1. Particle Size Distribution.

Section S2: Dimensions Analysis of the Nanorod Shell

Figure S2 presents the length distribution of the outermost nanorods on the CIP@C@LM shell. The measured lengths range from 23 nm to 118 nm, with an average of 62 nm. This relatively broad size distribution strongly suggests the concurrent growth and coexistence of multiple distinct nanoscale phases, which aligns well with the in-situ formation mechanism of the α-

GaOOH and α-FeOOH dual-hydroxide heterostructures discussed in the main text.

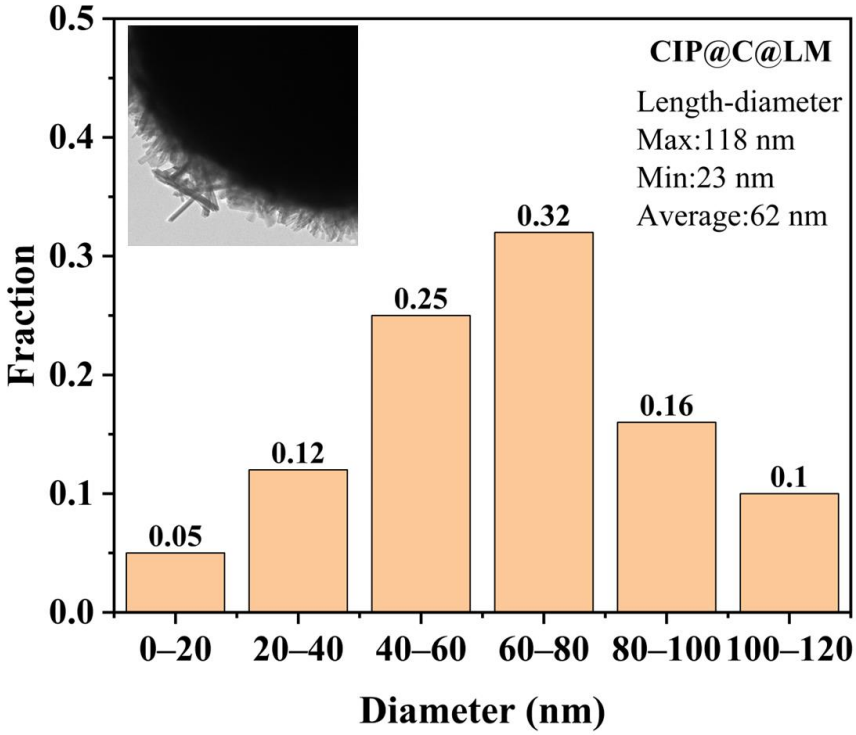

Figure S2. Dimensions Analysis of the Acicular Shell of CIP@C@LM

Section S3: SEM Characterization of Control Samples

To verify the critical role of the intermediate C layer, control experiments were conducted under identical processing conditions. As shown in Figures S3a–b, the direct ultrasonication of bare CIP in an aqueous environment leads to uncontrolled rapid oxidation, driven by the harsh sonochemical environment (e.g., localized hot spots and reactive radicals). This causes severe structural degradation and the irreversible consumption of the magnetic core. Conversely, the uniform, dual-hydroxide fibrous shell can only be successfully formed due to the presence of the intermediate C layer (Figs. S3c–d). Because the bare metallic surface lacks sufficient chemical affinity, the high-surface-tension LM tends to aggregate randomly rather than uniformly wet the particles. These comparative results unequivocally demonstrate the indispensable dual role of the C shell. Specifically, it acts as a robust protective barrier against ultrasonic-induced corrosion and serves as an essential interfacial template that lowers the interfacial energy, thereby guiding the uniform attachment and subsequent in-situ growth of the outer shell.

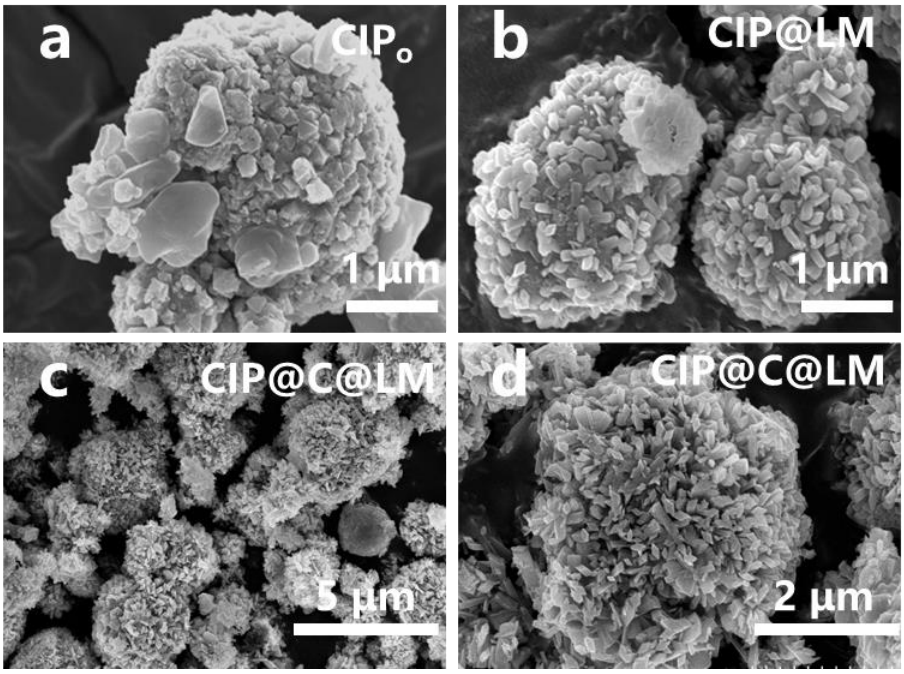

Figure S3. SEM of CIP_o (pristine CIP oxidized in water) (a), CIP@LM(b) and CIP@C@LM(c–d).

Section S4: Comparative EMW Absorption Performance of Control Samples

To further elucidate the roles of the C intershell and the ultrasonication time, the EMW absorption of several control samples was evaluated (Figure S4). CIP_o exhibits consistently poor absorption over the entire *f* range (Figure S4a), primarily due to the severe oxidation of CIP during direct sonication in water. Similarly, direct LM coating without the C intershell does not provide a bandwidth advantage. CIP@LM exhibits weakened performance (RL_{min} = −17.36 dB at 2.2 mm; EAB_{max} = 3.58 GHz over 12.66–16.24 GHz), indicating that without the C-mediated interfacial architecture, LM addition alone is insufficient to build effective dielectric pathways or optimize impedance matching.When the C shell is present, the degree of LM oxidation—controlled by ultrasonication time—becomes critical. For CIP@C@LM_1 (30 min), LM oxidation is limited (Figure S4b), retaining sufficient electrically active components to form a conductive network. Consequently, an RL_{min} of −44.14 dB is obtained at 9.84 GHz (2.0 mm), completely covering the X-band (Figure S4c), and the EAB_{max} reaches 6.61 GHz at 1.5 mm. However, excessive ultrasonication for 120 min (CIP@C@LM_2) produces additional rod-like byproducts (Figure S4d), indicating a higher oxidation degree and a larger fraction of insulating oxyhydroxide phases. This decreased electrical conductivity weakens the dielectric loss and deteriorates impedance matching, leading to much poorer EMW absorption (RL_{min} = −18.59 dB at 18 GHz with 5.5 mm; EAB_{max} = 2.63 GHz).

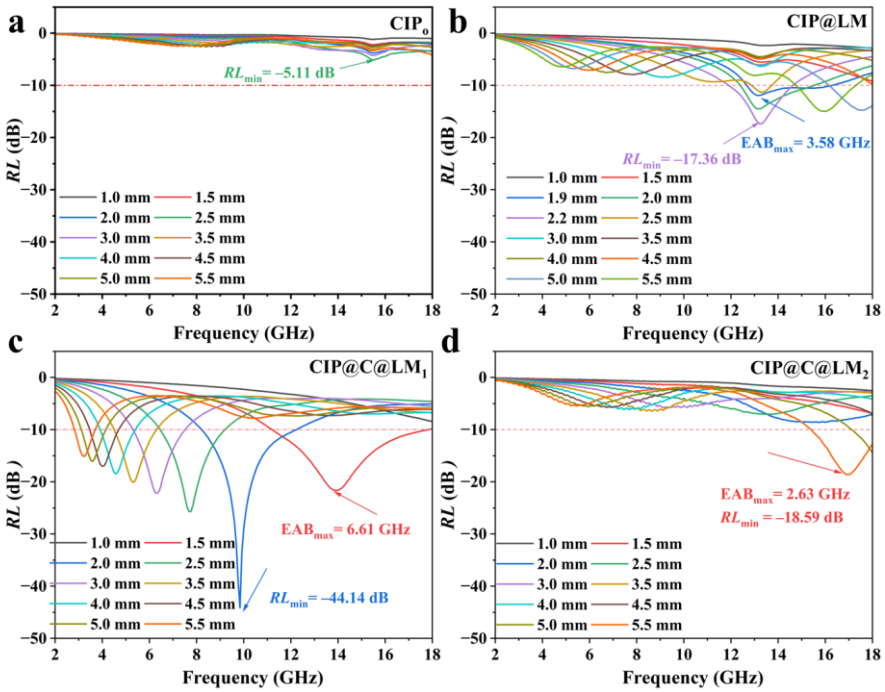

Figure S4. Comparison of EMW absorption characteristics of CIP_o(a), CIP@LM(b), $CIP@C@LM_1$(c) and $CIP@C@LM_2$(d)

Section S5: Electromagnetic Parameters of Samples at Different Ultrasonication Times

As shown in Figure S5a,b, both μ' and μ'' gradually decrease with increasing ultrasonication time. A weak resonance feature appears in the 60 min sample, which may arise from the magnetic coupling between the generated α-FeOOH and CIP, as further reflected in tan δ_μ (Figure S5c). In contrast, insufficient or excessive ultrasonication is unfavorable for constructing such an effective magnetic heterostructure. As shown in Figure S5d, ε' decreases markedly with prolonged ultrasonication. In particular, the nearly featureless ε' curve of the 120 min sample suggests the excessive generation of weakly conductive or nonconductive phases. In Figure S5e, ε'' of the 30 min sample continuously increases without a distinct relaxation peak, indicating that insufficient ultrasonication fails to establish the α-GaOOH-containing heterostructure and mainly alters the conductive response, resulting in limited polarization relaxation. By contrast, the 60 min sample exhibits a pronounced dielectric relaxation peak in ε'', which can be attributed to enhanced interfacial polarization and defect-induced dipolar polarization associated with the optimized heterostructure, thereby promoting electromagnetic energy dissipation. Furthermore, the comparison between tan δ_μ (Figure S5c) and tan δ_ε (Figure S5f), together with the frequency corresponding to RL_{min}, confirms that dielectric loss dominates the electromagnetic attenuation of the optimized sample.

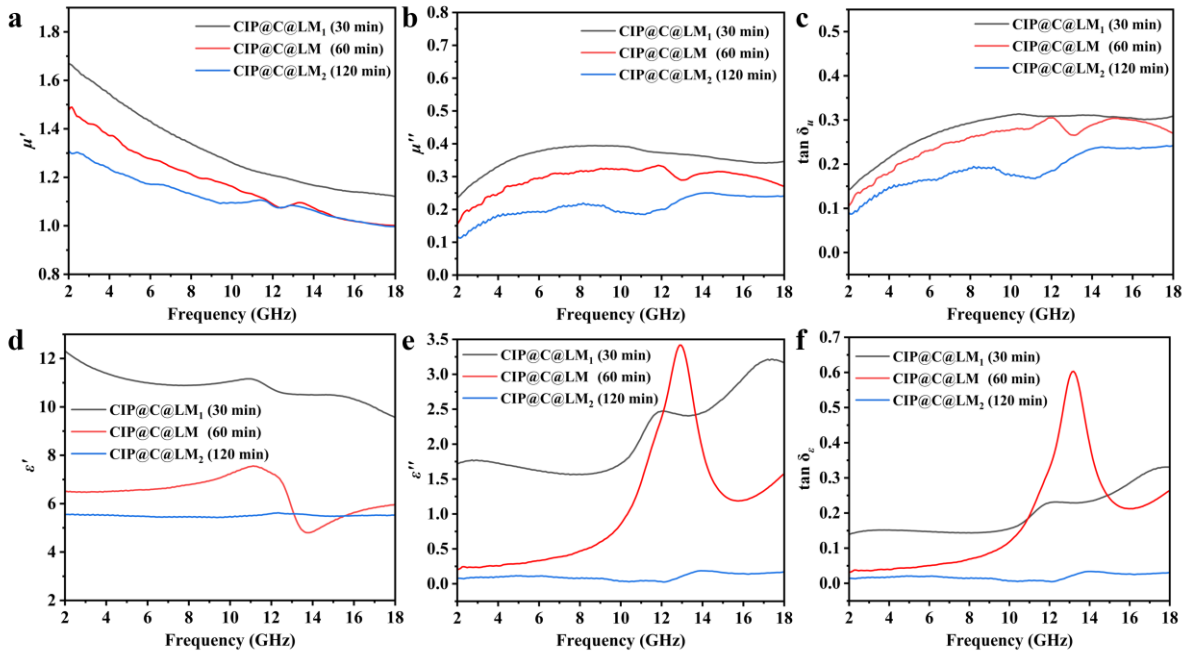

Figure S5. Comparison of the electromagnetic parameters of samples prepared with different ultrasonication durations: (a) real part of the complex permeability (μ'), (b) imaginary part of the complex permeability (μ''), (c) magnetic loss tangent (tan δ_μ), (d) real part of the complex permittivity (ε'), (e) imaginary part of the complex permittivity (ε''), and (f) dielectric loss tangent (tan δ_ε).

Section S6: Quantitative Analysis of Impedance Matching in the Absorption-Relevant Region

To quantitatively compare the impedance-matching behavior associated with broadband absorption, the frequency–thickness areas satisfying $0.8 < Z < 1.2$ were calculated within the thin-layer region of 1.5–2.5 mm. This thickness range covers the optimum thickness of CIP@C@LM and allows direct comparison of different frequency regions. As summarized in Table S1, within the full 2–18 GHz range, CIP@C@LM exhibits a matched area of 5.47 GHz·mm and a matched-area ratio of 34.19%, higher than those of CIP and CIP@C. In the 12–18 GHz region and the main absorption-relevant region of 10.44–18.00 GHz, CIP@C@LM also shows the highest matched-area ratios of 58.09% and 59.84%, respectively. These results confirm its favorable impedance matching in the thin-layer region directly associated with broadband absorption.

Table S1. Quantitative comparison of impedance matching within the thin-layer region of 1.5–2.5 mm

Frequency	CIP matched area / ratio	CIP@C matched area / ratio	CIP@C@LM matched area / ratio
2–18 GHz	3.12 GHz·mm / 19.50%	4.94 GHz·mm / 30.85%	5.47 GHz·mm / 34.19%
2–4 GHz	0.00 GHz·mm / 0.00%	0.00 GHz·mm / 0.00%	0.00 GHz·mm / 0.00%
4–8 GHz	0.19 GHz·mm / 4.85%	0.26 GHz·mm / 6.39%	0.2 GHz·mm / 4.92%
8–12 GHz	1.39 GHz·mm / 34.84%	2.29 GHz·mm / 57.25%	1.79 GHz·mm /44.7%
12–18 GHz	1.53 GHz·mm / 25.54%	2.39 GHz·mm / 39.83%	3.49 GHz·mm / 58.09%
10.44–18 GHz	2.14 GHz·mm / 28.37%	3.53 GHz·mm / 46.66%	4.52 GHz·mm / 59.84%

Note: The matched-area ratio was calculated using each selected frequency–thickness region as the reference area. The impedance-matched region was defined as $0.8 < Z < 1.2$.

Section S7: Reflection-Loss Performance at Reduced Filler Loadings

To evaluate the influence of filler loading on EMW absorption, the reflection-loss performances of CIP and CIP@C@LM at reduced filler loadings of 30 and 50 wt.% were further investigated, as shown in Figure S6. At 30 wt.%, pristine CIP exhibits negligible absorption, while CIP@C@LM shows an enhanced but still limited attenuation response. At 50 wt.%, both samples display improved absorption behavior, and CIP@C@LM exhibits a deeper reflection-loss minimum than CIP. Nevertheless, the absorption performance at these reduced filler loadings remains inferior to that of 60 wt.% CIP@C@LM presented in the main manuscript. These results indicate that the heterostructure improves the absorption response relative to pristine CIP, while sufficient filler loading is still required to achieve strong and broadband effective absorption in the present system.

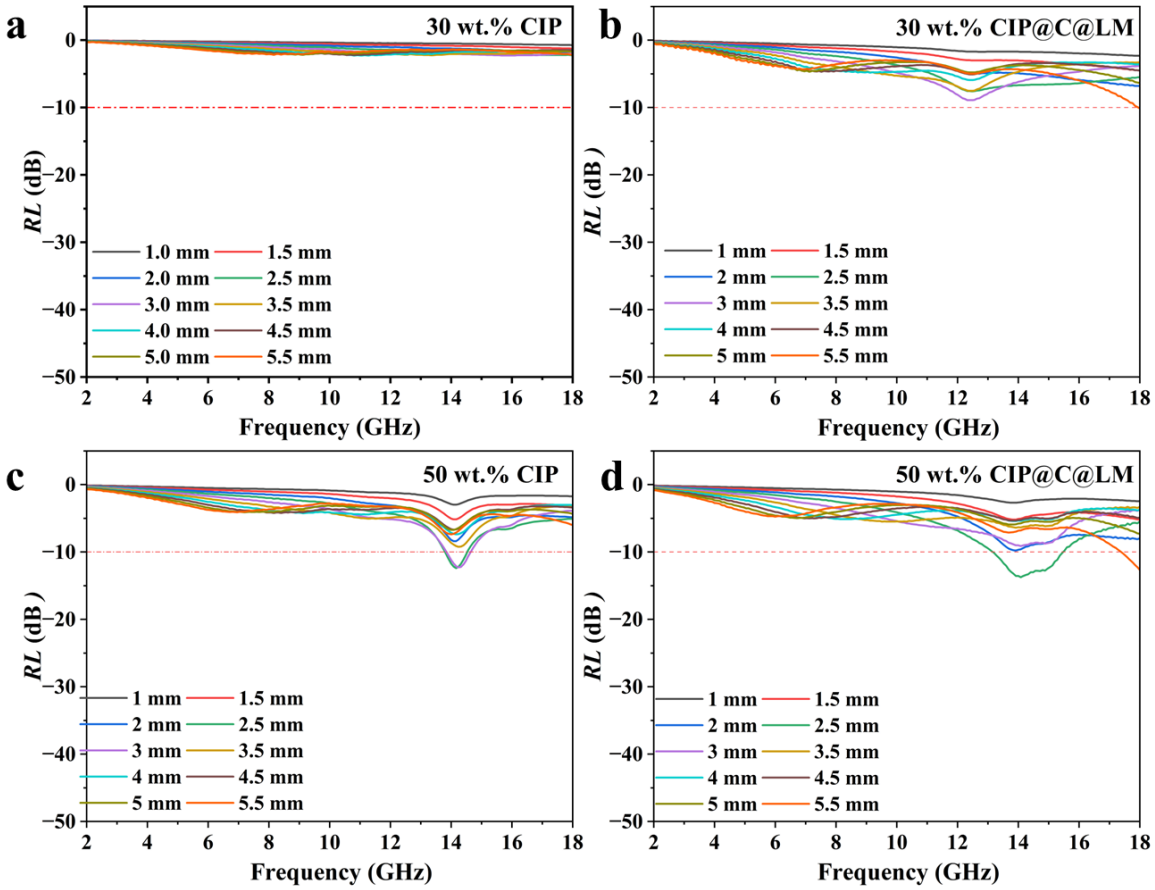

Figure S6. Reflection-loss curves of CIP and CIP@C@LM composites at reduced filler loadings: (a) 30 wt.% CIP, (b) 30 wt.% CIP@C@LM, (c) 50 wt.% CIP, and (d) 50 wt.% CIP@C@LM. The results of the 60 wt.% samples are presented in the main manuscript for comparison.

Section S8: Separation of Dielectric Loss Components Based on Debye Relaxation Theory

Understanding the EMW absorption mechanism requires a detailed analysis of dielectric loss behavior. According to Debye relaxation theory [1], the imaginary part of the complex permittivity (ε'') consists of two main contributions: conduction loss (ε_c'') and polarization loss (ε_p''). ε_c'' originates from the motion of free carriers under an electric field and dominates in the low-frequency region. ε_p'' arises from dipole relaxation, interfacial polarization, and other polarization effects, typically observed over a broader frequency range. The formula is as follows [2,3]:

$$\varepsilon'' = \varepsilon_c'' + \varepsilon_p'' \quad \text{(Equation 1)}$$

$$\varepsilon_c'' = \frac{\sigma}{\omega \varepsilon_0} \quad \text{(Equation 2)}$$

$$\varepsilon_p^{''}=\frac{(\varepsilon_s-\varepsilon_\infty)\omega\tau}{1+(\omega\tau)^2} \quad \text{(Equation 3)}$$

where ε_s is the static permittivity, ε_∞ is the high-f limit permittivity, $\omega = 2\pi f$ is the angular frequency, τ is the relaxation time, σ is the electrical conductivity, and ε_0 is the vacuum permittivity (8.85×10^{-12} F·m^{-1}). In the low f region, ε_c'' dominates due to the increasing contribution of the $\sigma / (\omega\varepsilon_0)$ term, which leads to a characteristic inverse relationship between ε'' and f. Assuming a constant electrical conductivity, ε'' is approximately proportional to $1/f$, enabling the extraction of the conduction loss component via linear fitting. The polarization loss can then be obtained by subtracting ε_c'' from the total ε''. In the high-f region, ε_c'' becomes negligible, and ε'' is primarily governed by dipolar relaxation processes, often manifested as f-dependent peaks in ε'' and dielectric loss tangent ($\tan\delta_\varepsilon$). These relaxation behaviors can also be visualized using Cole-Cole plots (ε'' vs ε'), where each semicircle corresponds to an individual relaxation process. The presence of multiple semicircles indicates multiple dipolar or interfacial polarization mechanisms contributing to dielectric loss.

Section S9: Tafel Curve Calculation

The potentiodynamic polarization parameters extracted from the Tafel plots in 3.5 wt.% NaCl solution (Table S2) further elucidate the excellent anti-corrosion properties of the final composite. Compared to pristine CIP ($I_{corr} = 3.16 \times 10^{-6}$ A, $E_{corr} = -0.415$ V), the CIP@C@LM heterostructure exhibits a significantly lower corrosion current (1.28×10^{-7} A) and a more positive corrosion potential –0.301 V). This substantial decrease in I_{corr} by over an order of magnitude, coupled with the anodic shift in E_{corr}, unequivocally demonstrates the synergistic protective effect of the inner C shell and the outer defect-rich dual-hydroxide layer. These hierarchical shells effectively block the penetration of corrosive species (H_2O, O_2, and Cl^-), thereby significantly boosting the environmental stability of the magnetic core for practical applications.

Table S2. Results of Tafel analysis for CIP, CIP@C and CIP@C@LM in 3.5 wt% NaCl solution

Samples	CIP	CIP@C	CIP@C@LM
I_{corr} (A)	3.16×10^{-6}	1.99×10^{-7}	1.28×10^{-7}
E_{corr} (V)	–0.415	–0.319	–0.301
β_a (V)	–8	–14.5	–27.5
β_c (V)	–13	13	17

$I_{corr:}$ Corrosion Current, E_{corr}: Corrosion Potential, $\beta_{a:}$ Anodic Tafel slope, β_c: Cathodic Tafel slope

REFERENCES

1. Kremer, F.; Kipnusu, W. K.; Fränzl, M. Orientation polarization spectroscopy—toward an atomistic understanding of dielectric relaxation processes. *Int. J. Mol. Sci.* **2022**, *23*, 8254. DOI: 10.3390/ijms23158254.
2. Qin, M.; Zhang, L.; Wu, H. Dielectric loss mechanism in electromagnetic wave absorbing materials. *Adv. Sci.* **2022**, *9*, 2105553. DOI: 10.1002/advs.202105553.
3. Zhang, K.; Yan, Y.; Wang, Z.; Ma, G.; Jia, D. Integration of electrical properties and polarization loss modulation on atomic Fe–N-RGO for boosting electromagnetic wave absorption. *Nano-Micro Lett.* **2025**, *17*, 46. DOI: 10.1007/s40820-024-01518-x.
4. Wu, N.; Liu, X.; Zhao, C.; Cui, C.; Xia, A. Effects of particle size on the magnetic and microwave absorption properties of carbon-coated nickel nanocapsules. *J. Alloys Compd.* **2016**, *656*, 628–634. DOI: 10.1016/j.jallcom.2015.10.027.